Eleventh International Conference on Computational Fluid Dynamics (ICCFD11), Maui, Hawaii, July 11-15, 2022

ICCFD11-2022-4102

Direct numerical simulation of droplet-laden homogeneous shear turbulence: numerical method and flow physics

P. Trefftz-Posada, A. Ferrante
Corresponding author: ferrante@aa.washington.edu

William E. Boeing Department of Aeronautics and Astronautics
University of Washington, Seattle, WA 98195, USA

Abstract: We have developed an explicit and direct pressure-correction method (FastRK3P*) to solve the incompressible Navier Stokes equations for two-fluid flows under shear-periodic boundary conditions. FastRK3P* preserves stability for simulating droplet-laden homogeneous shear turbulence (DLHST), while still requiring only one solution of the Poisson equation for pressure per time step. Using FastRK3P* coupled with the volume of fluid method (VoF), we have performed direct numerical simulations (DNS) of DLHST. The turbulent flow is at an initial Reynolds number based on Taylor microscale $Re_{\lambda_0} = 40$, and is initially laden with 1,258 droplets of diameter approximately equal to twice the Taylor length-scale of turbulence, resulting in a 5% droplet volume fraction. The droplet-to-fluid density and viscosity ratios are both equal to 10. In the present work, our objective is to determine the effects of varying the Weber number, We, and the shear number, Sh, on the budget of the turbulence kinetic energy (TKE). DNS results show the effects of the mean shear on droplet dynamics for different We, how this affects the terms of the TKE equation, and, thus, explain the evolution of TKE in DLHST.

Keywords: Direct Numerical Simulation, Turbulent Shear Flow, Shear-periodic Boundary Conditions, Droplet-Laden Flow, Multiphase Flow.

1 Introduction

For decaying isotropic turbulence laden with droplets of initial diameter of Taylor length-scale size, Dodd & Ferrante [1], through direct numerical simulations (DNS), explained the physical mechanisms of droplet/turbulence interaction and the pathways of turbulence kinetic energy (TKE) between droplets, carrier fluid, and the interface between the two. The DNS results of Dodd & Ferrante [1] showed that that the droplet-carrier-fluid interface represents a sink or source of TKE through the power of the surface tension, Ψ'_σ, due to the fluctuating velocity. Ψ'_σ acts as a sink (source) of TKE when the total surface area of the interface increases (decreases). In decaying isotropic turbulence, the absence of mean shear translates into absence of production of TKE due to shear. Thus, the next step of complexity from the study of [1] is studyingthe effects of shear on droplets and the effects of droplets on the production of TKE by simulating droplet-laden homogeneous shear turbulence (DLHST).

The studies of Rosti *et al.* and Scapin *et al.* [2, 3] advanced the numerical solution of single-phase homogeneous shear turbulence (HST) until a statistically-stationary (SS) state was reached, at which point droplets were injected. In nature, homogeneous shear turbulence exhibits unbounded growth of the integral length-scale and of TKE. SS-HST simulations artificially contain the length scales and exhibit 'bursting' of TKE. Because of the artificial 'bursting' of TKE exhibited, and the forcing in SS-HST, the effects of droplets/turbulence interaction are camouflaged and, thus, SS-HST should not be used for studying the physical mechanisms of the interactions between droplets and HST. Also, in Rosti *et al.* [2], the second-order

Adams-Bashforth (AB2) scheme was used for integrating in time the discretized Navier-Stokes equations of SS-HST. This scheme is not suitable for DNS of HST due to its weak instability, as recognized by Schumann [4] and proven by Kasbaoui *et al.* [5]. This weak instability creates fluctuations in the spectrum of turbulence kinetic energy at high wave-numbers, as shown in Fig. 1. In [3], a modified Adams-Bashforth scheme was proposed which addresses this instability, but adds an extra shear-remapping operation.

We have developed a new numerical method for simulating DLHST called FastRK3P*. This method combines FastP* [6] with FastRK3 [7]. FastRK3 is a third-order Runge-Kutta (RK3) pressure-correction method to solve the incompressible Navier-Stokes equations whilesolving the Poisson equation for pressure only once per time step vs. three times of the standard RK3 methodology [8]. Thus, the main two advantages of FastRK3P* are that it doesn't require the solution from the previous time step like AB2 (therefore preserving stability for simulating DLHST [5]), and only requires one solution of the Poisson equation for pressure per time step.

In the present work, we consider finite-size droplets larger than Taylor length scale size at the time of injection ($D_0 \approx 2\lambda_0$, where λ is the Taylor length scale, and the subscript 0 means at droplet injection time) in homogeneous shear turbulence. We ensure that the HST simulation is physically meaningful by monitoring the changes of the length scales and of the two-point velocity autocorrelation. Studying DLHST via DNS, after the work of Dodd & Ferrante [1] for droplet-laden decaying isotropic turbulence, is aimed to understanding the role of the mean shear on droplet/turbulence interaction and the modulation of TKE, e.g., how does the mean shear modulate the droplets interface, the power of surface tension, and how do the droplets affect the production of TKE.

We perform a parametric study of DNS of DLHST in which we vary the Weber number based on the r.m.s. velocity of turbulence ($We_{rms} = D_0 U_{rms}^2 \rho_c/\sigma$) and the shear number ($Sh = S/(U_{rms}/l)$), where D_0 is the initial droplet diameter, U_{rms} is the r.m.s. of the velocity fluctuations, ρ_c is the density of the carrier fluid, σ is the surface tension coefficient, $S = \partial \overline{U}_x/\partial z$ is the mean velocity gradient (which is constant), $\overline{U}_x$ is the mean velocity in the x–direction (which is linear), and l is the integral length scale.

2 Mathematical description

2.1 Governing equations

The non-dimensional governing equations for an incompressible flow of two immiscible fluids with mean shear in the absence of gravity are

$$\nabla \cdot \mathbf{u} = 0, \tag{1a}$$

$$\frac{\partial \mathbf{u}}{\partial t} = -\nabla \cdot (\mathbf{u}\mathbf{u}) - Sz\frac{\partial \mathbf{u}}{\partial x} - Su_3\hat{\mathbf{i}} + \frac{1}{\rho}\left[-\nabla p + \frac{1}{Re}\nabla \cdot (2\mu \mathbf{S}') + \frac{1}{We}\mathbf{f}_\sigma\right] \tag{1b}$$

where $\mathbf{u} = \mathbf{u}(\mathbf{x}, t)$ is the fluid fluctuating velocity, $S = \frac{\partial \overline{U}_x}{\partial z}$ is the mean shear rate where $\overline{U}_x$ is the mean velocity, $p = p(\mathbf{x}, t)$ is the pressure, $\rho = \rho(\mathbf{x}, t)$ is the density, $\mu = \mu(\mathbf{x}, t)$ is the dynamic viscosity, $\mathbf{S}' = \mathbf{S}'(\mathbf{x}, t)$ is the strain-rate tensor of the fluctuating velocity ($\mathbf{S}' = \frac{1}{2}[\nabla \mathbf{u} + (\nabla \mathbf{u})^T]$). *Re* and *We* are the Reynolds and Weber numbers, respectively, which are defined as:

$$Re = \frac{\tilde{U}\tilde{L}\tilde{\rho}_c}{\tilde{\mu}_c}, \qquad We = \frac{\tilde{\rho}_c \tilde{U}^2 \tilde{L}}{\tilde{\sigma}}, \tag{2}$$

where $\tilde{U}$, $\tilde{L}$, $\tilde{\rho}_c$, $\tilde{\mu}_c$ and $\tilde{\sigma}$ denote, in order, the reference dimensional velocity, length, carrier-fluid density, carrier-fluid dynamic viscosity and surface tension coefficient used to non-dimensionalize the governing equations (1a) and (1b). The subscripts c and d indicate the carrier fluid and droplet fluid, respectively. $\mathbf{f}_\sigma = \mathbf{f}_\sigma(\mathbf{x}, t)$ is the force per unit volume due to surface tension,

$$\mathbf{f}_\sigma = \kappa \delta(s)\mathbf{n} \tag{3}$$

where $\kappa = \kappa(\mathbf{x}, t)$ is the curvature of the droplet interface, $\mathbf{n} = \mathbf{n}(\mathbf{x}, t)$ is the unit vector that is normal to the interface and directed towards the interior of the droplet, δ is the Dirac δ-function that is needed to impose

$\mathbf{f}_\sigma$ only at the interface position and s is a normal coordinate centered at the interface, such that $s = 0$ at the interface.

2.2 Numerical method

In S2.2.1 we describe the FastRK3* method that is used to solve numerically the two-fluid governing equations (1a) and (1b). This method is coupled to the VoF method presented in S2.2.2, which is used to capture the motion of the droplet interface.

2.2.1 FastRK3P*

We solve the governing equations (1a) and (1b) throughout the whole computational domain, including the interior of the droplets. The domain is a rectangular prism with non-dimensional side lengths $(L_x, L_y, L_z) = (2, 1, 1)$. The governing equations are discretized in space in an Eulerian framework using the second-order central difference scheme on a uniform staggered mesh.

The solution algorithm begins by advecting the volume fraction of the droplet fluid, $C(\mathbf{x}, t)$, based on the known velocity field $\mathbf{u}^n$. The volume fraction has value $C = 0$ in the carrier fluid, $C = 1$ in the droplet fluid and $0 < C < 1$ in cells containing the droplet interface. After computing C^{n+1} (S2.2.2), the density and viscosity can be computed at time level $n + 1$.

Runge-Kutta methods are a family of multi-step iterative methods that construct approximate velocities at intermediate time steps, starting with the velocity at time level n, to obtain the velocities at time level $n + 1$. First, the computation of the approximate velocity omits the pressure term in (1b), and the second term on the right-hand side in (1b) is omitted. This term represents the advection of momentum by the mean velocity, and is accounted for later in the solution algorithm by a 'shear-remapping' operation. The momentum operator for the right-hand side of (1b) with the omitted terms is defined as

$$\mathcal{M}(\mathbf{u}) = -\nabla \cdot (\mathbf{u}\mathbf{u}) - S u_3 \hat{\mathbf{i}} + \frac{1}{Re}\left[\frac{1}{\rho^{n+1}}\nabla \cdot \left(2\mu^{n+1}\mathbf{S}'\right)\right] + \frac{1}{We}\left[\frac{\kappa^{n+1}\nabla C^{n+1}}{\bar{\rho}}\right], \tag{4}$$

where surface tension force, $\mathbf{f}_\sigma$, of (1b) has been substituted by using Brackbill's continuum surface force (CSF) approach.

The solution algorithm proceeds by calculating three intermediate velocities for the three stages of the RK3 algorithm using the FastRK3 method of [7] as:

$$\mathbf{u}_1^* = \mathbf{u}^n + \frac{1}{3}\Delta t \mathcal{M}(\mathbf{u}^n) \tag{5}$$

$$\mathbf{u}_2^* = \mathbf{u}^n + \Delta t\left[-\mathcal{M}(\mathbf{u}^n) + 2\mathcal{M}\left(\mathbf{u}_1^* - \frac{1}{3}\Delta t\frac{\nabla\phi_1}{\rho^{n+1}}\right)\right] \tag{6}$$

$$\mathbf{u}_3^* = \mathbf{u}^n + \Delta t\left[\frac{3}{4}\mathcal{M}\left(\mathbf{u}_1^* - \frac{1}{3}\Delta t\frac{\nabla\phi_1}{\rho^{n+1}}\right) + \frac{1}{4}\mathcal{M}\left(\mathbf{u}_2^* - \frac{1}{3}\Delta t\frac{\nabla\phi_2}{\rho^{n+1}}\right)\right], \tag{7}$$

where the $\nabla\phi$ terms represent a pressure-like field that correct $\mathbf{u}_1^*$ and $\mathbf{u}_2^*$ to be approximately divergence-free. For FastRK3P* these terms are defined as

$$\frac{\nabla\phi_1}{\rho^{n+1}} = \left[\frac{\nabla p}{\rho}\right]^n \tag{8}$$

$$\frac{\nabla\phi_2}{\rho^{n+1}} = \left[\frac{\nabla p}{\rho}\right]^n. \tag{9}$$

The choice of constant extrapolation of pressure to determine the $\nabla\phi$ terms reduces the temporal accuracy of the modified RK3 method from third-order to second-order, but it removes the dependence on solutions from previous time steps. The right-hand side of equations (8) and (9) are computed and stored at each

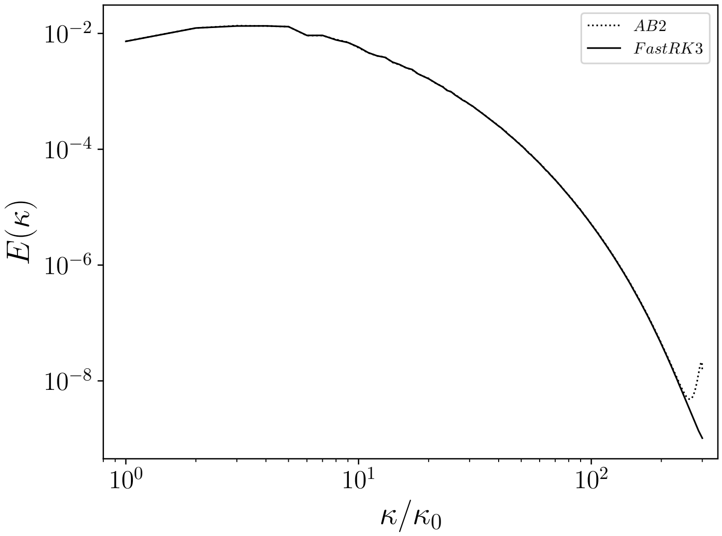

Figure 1: Spectrum of TKE, $E(\kappa)$, for single-phase HST at $S \cdot t = 6$ for AB2 (dotted line) and FastRK3 (solid line) time-integration schemes. The wavenumber, κ, is normalized by the lowest non-zero wavenumber, $\kappa_0 = 2\pi/\mathcal{L}$.

time step according to the FastP* [6] pressure splitting as

$$\left[\frac{\nabla p}{\rho}\right]^n = \frac{1}{\rho_0}\nabla p^n + \left(\frac{1}{\rho^n} - \frac{1}{\rho_0}\right)\nabla p^*, \tag{10}$$

where $p^* = 2p^n - p^{n-1}$. Next, the advection by the mean velocity is accounted for by the 'shear-remapping' operator which maps local values of velocity to value computed upstream according to the magnitude of the local mean velocity by using spectral interpolation. The advection of mean velocity is, thus, applied to $\mathbf{u}_3^*$ with the 'shear-remapping' operator as

$$\breve{\mathbf{u}}_3^* = \mathbf{u}_3^*(\mathbf{x} - \Delta t S z \hat{\mathbf{i}}) \tag{11}$$

The pressure is computed by solving the Poisson equation [6]:

$$\nabla^2 p^{n+1} = \nabla \cdot \left[\left(1 - \frac{\rho_0}{\rho^{n+1}}\right)\nabla p^*\right] + \frac{\rho_0}{\Delta t}\nabla \cdot \breve{\mathbf{u}}_3^*, \tag{12}$$

where we have split the pressure gradient term [9] as

$$\frac{1}{\rho^{n+1}}\nabla p^{n+1} \to \frac{1}{\rho_0}\nabla p^{n+1} + \left(\frac{1}{\rho^{n+1}} - \frac{1}{\rho_0}\right)\nabla p^*, \tag{13}$$

where $\rho_0 = \min(\rho_1, \rho_2)$. The advantage of using (13) is that it yields a constant coefficient Poisson equation (12) which can be solved efficiently using direct methods. Equation (12) is solved directly using a combination of a two-dimensional fast Fourier transform (FFT) in the x-y plane and Gaussian elimination in the z-direction [10]. Finally, we update the velocity field to find $\mathbf{u}^{n+1}$ by applying the pressure-correction to $\breve{\mathbf{u}}_3^*$ as

$$\mathbf{u}^{n+1} = \breve{\mathbf{u}}_3^* - \Delta t\left[\frac{1}{\rho_0}\nabla p^{n+1} + \left(\frac{1}{\rho^{n+1}} - \frac{1}{\rho_0}\right)\nabla p^*\right] \tag{14}$$

Figure 1 shows the difference in the turbulence kinetic energy spectra when using AB2 versus FastRK3 method to simulate case A_2. The spectra from the AB2 method shows unphysical fluctuations at higher wavenumbers, while the spectra from the FastRK3 method decays smoothly as expected.

2.2.2 Volume-of-fluid method

In the VoF method, the sharp interface between the two immiscible fluids is determined using the VoF color function, C, which represents the volume fraction of the droplet fluid in each computational cell. In our VoF method, the interface between the two fluids is reconstructed using a piecewise linear interface calculation (PLIC) [11]. The interface reconstruction in each computational cell consists of two steps: the computation of the interface normal $\mathbf{n} = (n_x, n_y, n_z)$ and the computation of the interface location. The algorithm that we use to evaluate the interface normal is a combination of the centered-columns method [12] and Youngs' method [11] known as the mixed-Youngs-centered (MYC) method [13].

If we consider a characteristic function χ that has value $\chi = 1$ in the droplet fluid and $\chi = 0$ in the carrier fluid, χ is governed by the following advection equation:

$$\frac{\partial \chi}{\partial t} + \mathbf{u} \cdot \nabla \chi = 0. \tag{15}$$

The volume fraction $C_{i,j,k}$ of grid cell i, j, k is related to the characteristic function χ by the integral relation

$$C_{i,j,k}(t) = \frac{1}{V_0} \iiint_{V_0} \chi(\mathbf{x}, t) d\mathbf{x}, \tag{16}$$

where V_0 is the volume of the i, j, k cell. The volume fraction C is advanced in time using the advection algorithm of [14], which is mass conserving, and wisps are redistributed and suppressed using the method of [15].

2.2.3 Shear-periodic boundary conditions

In homogeneous shear turbulence, periodic boundary conditions are applied in the streamwise x-direction, and spanwise y-direction. In the z-direction, in which the mean carrier-flow velocity varies, the shear creates time dependent boundary conditions, such that, for a generic dependent variable f, the shear-periodic boundary conditions are expressed as

$$f(x, y, L_z, t) = f(x - S \cdot tL_z, y, 0, t). \tag{17}$$

Depending on the choice of S and time step, the x position of the right-hand side of (17) may fall in between grid points. For velocity and pressure, pseudo-spectral interpolation is used to interpolate between grid points. However, the VoF variables (such as the interface normal, plane constant, and curvature) cannot be interpolated pseudo-spectrally.

All VoF variables are located at cell centers along with the pressure field, while velocities are located at the staggered cell faces. FastRK3P* computes the momentum operator at staggered grid locations. In order to solve (1b) numerically, the surface tension term, $\mathbf{f}_\sigma$, must be computed on the staggered grid through averaging. 'Ghost cells' are used to calculate $\mathbf{f}_\sigma$ on the staggered mesh. With regular periodic boundary conditions, the value of $\mathbf{f}_\sigma$ can be copied directly from the source cell in the interior domain into the destination 'ghost cell'. A simple copy is not possible with shear-periodic boundary conditions because the x value for the source cell may not be located on the grid. To obtain the necessary 'ghost cell' values of VoF variables, the algorithm copies a slab that is four grid points thick at the vertical boundaries of the interior domain to copy into the destination 'ghost cells'. Next, the VoF advection algorithm is employed to shift these 'ghost cells' by the corresponding distance in x according to Eq. (17). Finally, the interfaces are reconstructed and the curvature is computed so that it can be used to calculate $\mathbf{f}_\sigma$ on the staggered mesh.

Case	We_{rms}	$\varphi \equiv \rho_d/\rho_c$	$\gamma \equiv \mu_d/\mu_c$	ϕ_m	ϕ_v	We	S
A_2	–	–	–	0	0	–	5
A_4	–	–	–	0	0	–	10
B_2	0.02	10	10	0.5	0.05	16.19	5
B_4	0.02	10	10	0.5	0.05	12.65	10
C_2	0.1	10	10	0.5	0.05	80.95	5
C_4	0.1	10	10	0.5	0.05	63.24	10
D_2	0.5	10	10	0.5	0.05	404.73	5
D_4	0.5	10	10	0.5	0.05	316.18	10

Table 1: Simulation properties (dimensionless) at droplet release.

3 Results and discussion

3.1 Initial conditions and droplet properties

3.1.1 Carrier flow parameters and initial conditions

The initial turbulent velocity field is generated by prescribing the TKE spectrum, $E(\kappa)$ as [16, Sec. 6.5.3], and ensuring that it is isotropic, divergence-free with respect to the discretized form of the continuity equation and that the velocity cross-correlation spectra, $R_{ij}(\kappa)$, satisfy the realizability constraint [17].

The initial velocity field is allowed to develop with periodic boundary conditions and without shear (i.e., as decaying isotropic turbulence), until the skewness of the velocity derivative S_u has reached ≈ -0.50, then, a constant mean velocity gradient $S = 5$ or $S = 10$, which correspond to $Sh \approx 2$ and $Sh \approx 4$, respectively, is imposed on the flow. In order to ensure our simulations are physically meaningful, we ensure that $\eta\kappa_{max} \geq 1$ at all times, where $\kappa_{max} = \pi N$ is the maximum resolved wavenumber and $N = 600$ is the number of grid points in the y and z-directions, while $N_x = 2N$. Additionally, we ensure that the two point Eulerian velocity autocorrelation in the x-direction diminishes to zero in less than half the length of the domain length in x, L_x, at all times. To satisfy this condition, the domain length in the x-direction is double its length in the y and z-directions.

3.1.2 Droplet properties

We perform two simulations of droplet-free flow, A_2 and A_4, and eight simulations of DLHST (Table 1). Cases A_2^* and A_4^* are limiting cases in which the viscosity and density ratios are unity and the Weber number is infinity. We analyze the effects of varying the shear number Sh and the initial droplet Weber number based on the r.m.s. of velocity fluctuations (We_{rms}). In cases A_2–D_2, $Sh \approx 2$ while We_{rms} increases from 0.02 to 0.5, and, in cases A_4–D_4 $Sh \approx 4$, while We_{rms} increases from 0.02 to 0.5. The density and viscosity ratios for all droplet-laden cases are set to $\varphi = 10$ and $\gamma = 10$, respectively. For all cases, the droplet volume fraction is $\phi_v = 0.05$, the initial number of droplets is $N_d = 1260$, and the initial non-dimensional droplet diameter is $D_0 = 0.0533$.

The flow field evolves free of droplets until $S \cdot t = 2$ which corresponds to one flow-through of the mean shear velocity. At that time, droplets are randomly seeded at rest in the domain under the constraint that the distance between droplet centers must be at least $2.1D_0$.

3.2 Turbulence kinetic energy equations

In order to explain the fundamental physical mechanisms of the interactions of droplets with HST, we start by analyzing the evolution equation of TKE, $k(t)$, for the two-fluid flow, $k_c(t)$ for the carrier-fluid flow, and $k_d(t)$ for the droplet-fluid flow .

The evolution equation of $k(t)$ is

$$\frac{\mathrm{d}k}{\mathrm{d}t} = \mathcal{P} - \varepsilon + \Psi'_\sigma \tag{18}$$

where

$$k(t) \equiv \frac{1}{2}\langle \rho u_j u_j \rangle, \tag{19a}$$

$$\mathcal{P}(t) \equiv -S\langle \rho u_1 u_3 \rangle, \tag{19b}$$

$$\varepsilon(t) \equiv \frac{1}{Re}\langle T'_{ij} S'_{ij} \rangle, \tag{19c}$$

$$\Psi'_\sigma(t) \equiv \frac{1}{We}\langle u_j f_{\sigma,j} \rangle, \tag{19d}$$

where $\langle \cdots \rangle$ denotes instantaneous spatial-averaging over the entire computational domain. $T'_{ij} = 2\mu S'_{ij}$ is the viscous stress tensor, and S'_{ij} is the strain-rate tensor of the fluctuating velocity defined in S2.1. In (19d), $\mathcal{P}(t)$ is the production of $k(t)$, $\varepsilon(t)$ is the dissipation rate of $k(t)$, and $\Psi'_\sigma(t)$ is the power of the surface tension due to the fluctuating velocity.

The evolution equation for the TKE of the carrier-fluid flow, $k_c(t)$, is

$$\frac{\mathrm{d}k_c}{\mathrm{d}t} = \mathcal{P}_c - \varepsilon_c + T_{\nu,c} + T_{p,c}, \tag{20}$$

and the evolution equation for the TKE of droplet-fluid flow, $k_d(t)$, is

$$\frac{\mathrm{d}k_d}{\mathrm{d}t} = \mathcal{P}_d - \varepsilon_d + T_{\nu,d} + T_{p,d}. \tag{21}$$

The terms in (20) and (21) are defined as

$$\begin{aligned} k_c(t) \equiv \tfrac{1}{2}\langle \rho u_j u_j \rangle_c, \quad \mathcal{P}_c(t) \equiv -S\langle \rho u_1 u_3 \rangle_c, \quad \varepsilon_c(t) \equiv \frac{1}{Re}\langle \mathbf{T'}_{ij}\mathbf{S'}_{ij} \rangle_c, \\ T_{\nu,c}(t) \equiv \frac{1}{Re}\frac{\partial \langle \mathbf{T'}_{ij} u_j \rangle_c}{\partial x_i}, \quad T_{p,c}(t) \equiv -\frac{\partial \langle u_j p \rangle_c}{\partial x_j}, \end{aligned} \tag{22}$$

and

$$\begin{aligned} k_d(t) \equiv \tfrac{1}{2}\langle \rho u_j u_j \rangle_d, \quad \mathcal{P}_d(t) \equiv -S\langle \rho u_1 u_3 \rangle_d, \quad \varepsilon_d(t) \equiv \frac{1}{Re}\langle \mathbf{T'}_{ij}\mathbf{S'}_{ij} \rangle_d, \\ T_{\nu,d}(t) \equiv \frac{1}{Re}\frac{\partial \langle \mathbf{T'}_{ij} u_j \rangle_d}{\partial x_i}, \quad T_{p,d}(t) \equiv -\frac{\partial \langle u_j p \rangle_d}{\partial x_j}, \end{aligned} \tag{23}$$

where $\langle \ldots \rangle_c$ and $\langle \ldots \rangle_d$ denote spatial averaging over the carrier fluid and droplet fluid, respectively. In (22) and (23), $\mathcal{P}_c$ and $\mathcal{P}_d$ are the productions of TKE, ε_c and ε_d are the dissipation rates of TKE, $T_{\nu,c}$ and $T_{\nu,d}$ are the viscous powers, and $T_{p,c}$ and $T_{p,d}$ are the pressure powers. The power terms in (18), (20) and (21) are related through the identity

$$\Psi'_\sigma = (1-\phi_v)\left[T_{\nu,c} + T_{p,c}\right] + \phi_v\left[T_{\nu,d} + T_{p,d}\right]. \tag{24}$$

3.3 Comparison of TKE budget for droplet-free and droplet-laden turbulence

In this section, we present the effects of droplets on HST relative to the droplet-free case by analyzing the terms of the TKE budget equation (18) and, then, we explain the underlying physical mechanisms.

3.3.1 Two-fluid TKE Budget

Figure 2 shows the temporal evolution of $k(t)$ normalized by the initial value for the droplet-free cases at droplet release-time, k/k_0. The average rate of change of TKE after $S \cdot t > 4.25$ are calculated and shown. For cases B_2 and B_4, the rate of change of TKE is increased with respect to the droplet-free cases (A_2 and A_4). For cases C_2 and C_4, the rate of change of TKE oscillates near the value for the droplet-free cases. For cases D_2 and D_4, the rate of change of TKE is decreased with respect to the droplet free cases. For all

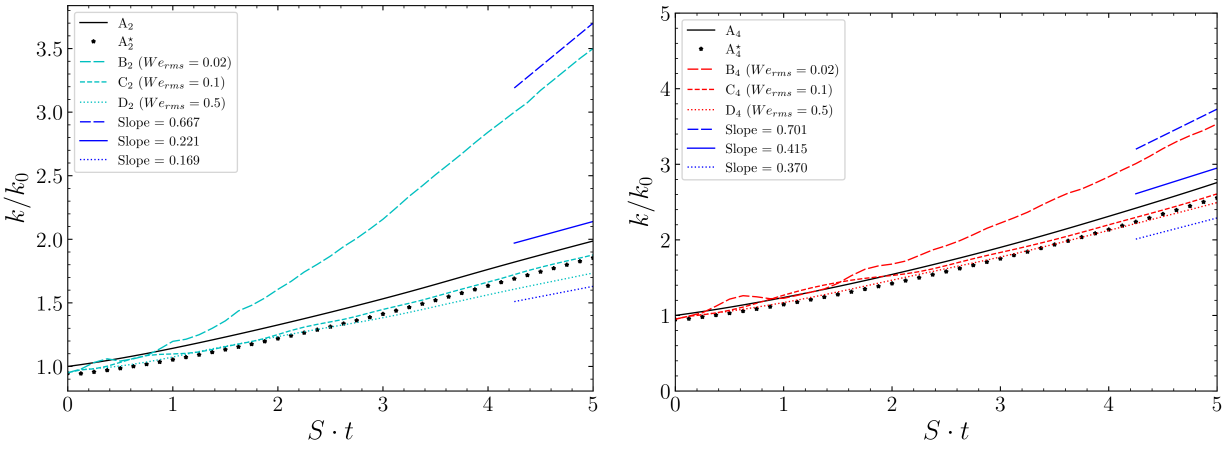

(a)

(b)

Figure 2: Temporal evolution of the turbulence kinetic energy, k, normalized by its value at droplet-release time, k_0.

droplet-laden cases, $\mathrm{d}(k/k_0)/\mathrm{d}t$ decreases with increasing We_{rms}.

To explain why droplets modify the rate of change of k, we analyze the temporal evolution of the terms on the right-hand side of (18), that is $\mathcal{P}$, ε, and Ψ'_σ. Figure 3 shows the temporal evolution of the production of TKE normalized by the initial dissipation rate of TKE for the droplet-free cases at droplet release-time, $\mathcal{P}/\varepsilon_0$. For cases B$_2$ and B$_4$, the production is increased with respect to the droplet free cases. For cases C$_2$ and C$_4$, the production closely matches that of the droplet free cases. For cases D$_2$ and D$_4$, the production is reduced with respect to the droplet free cases. For all droplet-laden cases, $\mathcal{P}$ decreases with increasing We_{rms}.

Figure 4 shows the temporal evolution of the normalized dissipation rate of TKE, $\varepsilon/\varepsilon_0$. For all droplet-laden cases, the dissipation rate is enhanced compared to the droplet-free cases, with an increasing We_{rms} leading to a decrease in the dissipation rate.

Figure 5 shows the temporal evolution of the power of the surface tension due to the fluctuating velocity normalized by the initial dissipation rate of TKE for the droplet-free cases at droplet release-time, $\Psi'_\sigma/\varepsilon_0$. For cases B$_2$ and B$_4$, Ψ'_σ oscillates around roughly 200% of the initial dissipation rate, ε_0, which corresponds to 30% of the instantaneous dissipation rate, ε, at $S \cdot t = 5$. Therefore in cases B$_2$ and B$_4$, Ψ'_σ represents a significant source of TKE for $S \cdot t > 2$. For cases C$_2$ and C$_4$, Ψ'_σ initially exhibits oscillations around zero up to 80% of ε_0 (case C$_2$) and 200% (case C$_4$), which decay to less than 17% (case C$_2$) and less than 25% (case C$_4$) of the instantaneous dissipation rate, ε, at $S \cdot t = 5$. For cases C$_2$ and C$_4$, Ψ'_σ represents a moderate source or sink of TKE for $0 < S \cdot t < 3$, and a more neutral role in the time evolution of the TKE for $S \cdot t > 3$. For cases D$_2$ and D$_4$, Ψ'_σ is limited to ±20% of the instantaneous dissipation rate, ε, thus playing a more neutral role in time evolution of the TKE.

4 Conclusions

We have developed a new numerical method, FastRK3P*, for simulating droplet-laden homogeneous shear turbulence that is stable for simulating HST unlike the second-order Adams-Bashforth scheme, and still only requires one solution of the Poisson equation per time step vs. three for standard RK3 methodologies. This method combines the advantages and progress made with FastP* for simulating two-fluid flows with FFT-based Poisson solver [6], with FastRK3 [7, 18] which solves the incompressible Navier-Stokes equations with an explicit RK3 method while solving the Poisson equation for pressure only once per time step. Using FastRK3P*, we have performed direct numerical simulations of homogeneous shear turbulence laden with deformable droplets, whose diameter is approximately equal to twice the Taylor lengthscale at the time of droplet release. The goal of the study was to explain the physical mechanisms of droplet-turbulence

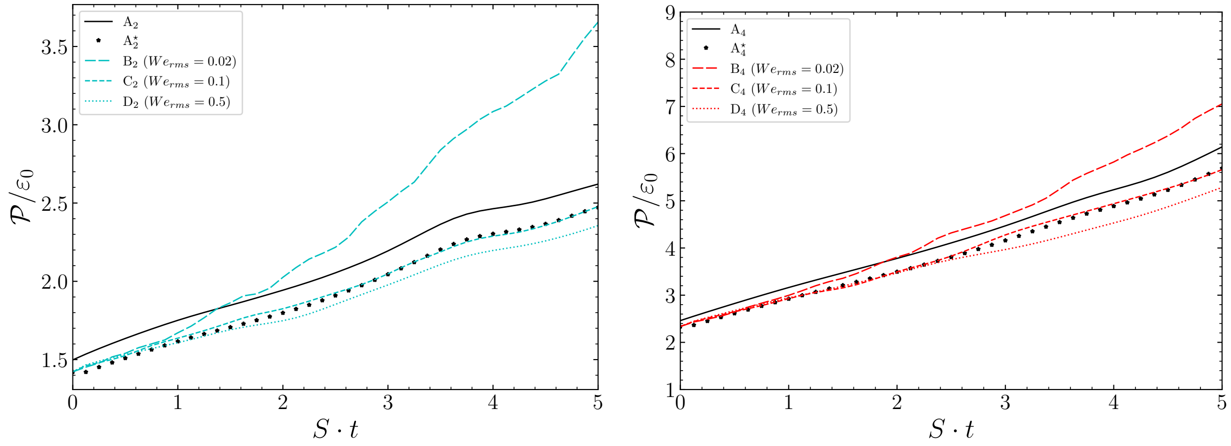

(a) (b)

Figure 3: Temporal evolution of the production of turbulence kinetic energy, $\mathcal{P}$, normalized by the value of the dissipation rate at droplet-release time, ϵ_0.

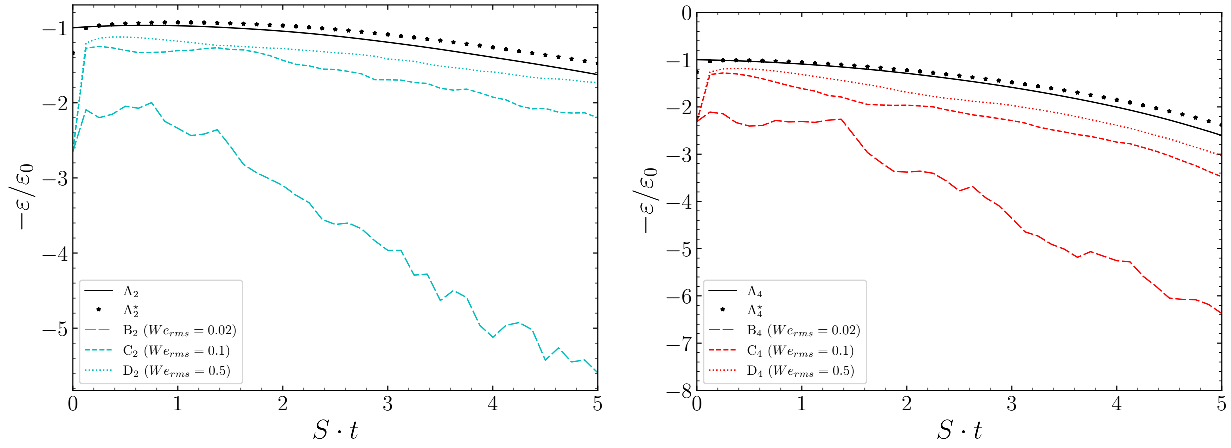

(a) (b)

Figure 4: Temporal evolution of the dissipation rate of turbulence kinetic energy, ϵ, normalized by its value at droplet-release time, ϵ_0.

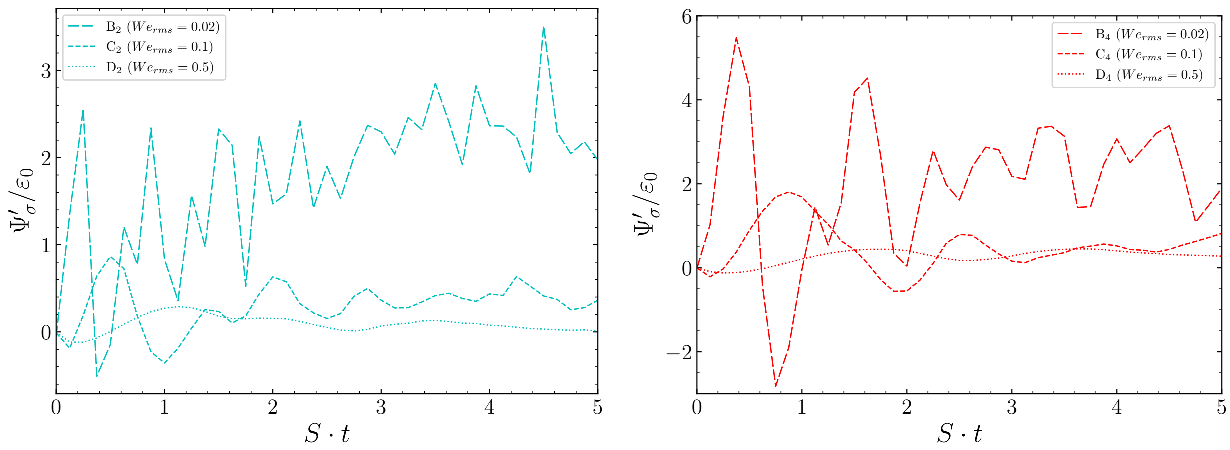

(a)

(b)

Figure 5: Temporal evolution of the power of the surface tension due to the fluctuating velocity, Ψ'_σ, normalized by the value of the dissipation rate at droplet-release time, ϵ_0.

interaction in the presence of shear for HST. Understanding these mechanisms is a prerequisite for developing predictive, physics-based turbulence models, e.g., Freud & Ferrante [19, 20].

We simulated six cases in which we released 1260 droplets from rest in homogeneous shear turbulence at an initial Reynolds number based on the Taylor lengthscale of $Re_\lambda = 40$. In each case we varied the Weber number ($0.02 \leq We_{\rm rms} \leq 0.5$), while the density and dynamic viscosity ratios between the droplet fluid and the carrier fluid were constant ($\rho_d/\rho_c = \mu_d/\mu_c = 10$). The governing equations were discretized and solved in a cubic domain using $1200 \times 600 \times 600$ grid points, and each droplet was resolved by 32 grid points across its diameter. The droplets were captured in time using the advection method of [14] and the wisp-suppression and redistribution method of [15].

We have applied our new numerical method to simulate six cases of DLHST, varying the shear number $Sh = S/(U_{rms}/l)$ and the initial droplet Weber number based on the r.m.s. of velocity fluctuations ($We_{rms} = D_0 U_{rms}^2 \rho_c/\sigma$). The findings of this study are summarized as follows:

1. For cases B$_2$ and B$_4$, the rate of change of TKE is increased with respect to the droplet-free cases (A$_2$ and A$_4$). For cases C$_2$ and C$_4$, the rate of change of TKE oscillates near the value for the droplet-free cases. For cases D$_2$ and D$_4$, the rate of change of TKE is decreased with respect to the droplet free cases. For all droplet-laden cases, $\mathrm{d}(k/k_0)/\mathrm{d}t$ decreases with increasing $We_{\rm rms}$.
2. For cases B$_2$ and B$_4$, the production is increased with respect to the droplet free cases. For cases C$_2$ and C$_4$, the production closely matches that of the droplet free cases. For cases D$_2$ and D$_4$, the production is reduced with respect to the droplet free cases. For all droplet-laden cases, $\mathcal{P}$ decreases with increasing $We_{\rm rms}$.
3. For all droplet-laden cases, the dissipation rate is enhanced compared to the droplet-free cases, with an increasing $We_{\rm rms}$ leading to a decrease in the dissipation rate.
4. For cases B$_2$ and B$_4$, Ψ'_σ represents a significant source of TKE for $S \cdot t > 2$. For cases C$_2$ and C$_4$, Ψ'_σ represents a moderate source or sink of TKE for $0 < S \cdot t < 3$, and a more neutral role in the time evolution of the TKE for $S \cdot t > 3$. For cases D$_2$ and D$_4$, Ψ'_σ plays a more neutral role in time evolution of the TKE.

Acknowledgements

The numerical simulations were performed in part on Hyak, high-performance computer cluster at UW, and in part on the Extreme Science and Engineering Discovery Environment (XSEDE, [21]) under XRAC Grant No. TG-CTS100024. XSEDE is supported by National Science Foundation Grant No. ACI-1053575.

We specifically acknowledge the Texas Advanced Computing Center (TACC) at The University of Texas at Austin (http://www.tacc.utexas.edu) and the San Diego Supercomputer Center (SDSC) at the University of California, San Diego (https://www.sdsc.edu/) for providing HPC resources that have contributed to the research results reported within this paper.

References

[1] M. S. Dodd and A Ferrante. On the interaction of Taylor lengthscale size droplets and isotropic turbulence. J. Fluid Mech., 806:356–412, 2016.

[2] M. E. Rosti, Z. Ge, S. S. Jain, M. S. Dodd, and L. Brandt. Droplets in homogeneous shear turbulence. J. Fluid Mech., 876:962–984, 2019.

[3] N. Scapin, F. Dalla Barba, G. Lupo, M. E. Rosti, C. Duwig, and L. Brandt. Finite-size evaporating droplets in weakly compressible homogeneous shear turbulence. J. Fluid Mech., 934, 2022.

[4] U. Schumann. Algorithms for direct numerical simulation of shear-periodic turbulence. In Ninth International Conference on Numerical Methods in Fluid Dynamics, pages 492–496. Springer, 1985.

[5] M. H. Kasbaoui, R. G. Patel, D. L. Koch, and O. Desjardins. An algorithm for solving the navier–stokes equations with shear-periodic boundary conditions and its application to homogeneously sheared turbulence. J. Fluid Mech, 833:687–716, 2017.

[6] M. S. Dodd and A. Ferrante. A fast pressure-correction method for incompressible two-fluid flows. J. Comput. Phys., 273:416–434, 2014.

[7] A. B. Aithal and A. Ferrante. A fast pressure-correction method for incompressible flows over curved walls. J. Comput. Phys., 421:109693, 2020.

[8] B. Sanderse and B. Koren. Accuracy analysis of explicit Runge-Kutta methods applied to the incompressible Navier-Stokes equations. J. Comput. Phys., 231(8):3041–3063, 2012.

[9] S. Dong and J. Shen. A time-stepping scheme involving constant coefficient matrices for phase-field simulations of two-phase incompressible flows with large density ratios. J. Comput. Phys., 231(17):5788–5804, 2012.

[10] H. Schmidt, U. Schumann, and H. Volkert. Three dimensional, direct and vectorized elliptic solvers for various boundary conditions. Rep. 84-15, DFVLR-Mitt, 1984.

[11] D. L. Youngs. Time-dependent multi-material flow with large fluid distortion. Numer. Methods Fluid Dyn., 1(1):41–51, 1982.

[12] G. H. Miller and P. Colella. A conservative three-dimensional Eulerian method for coupled solid–fluid shock capturing. J. Comput. Phys., 183(1):26–82, 2002.

[13] E. Aulisa, S. Manservisi, R. Scardovelli, and S. Zaleski. Interface reconstruction with least-squares fit and split advection in three-dimensional Cartesian geometry. J. Comput. Phys., 225(2):2301–2319, 2007.

[14] G. D. Weymouth and D. K-P Yue. Conservative volume-of-fluid method for free-surface simulations on Cartesian-grids. J. Comput. Phys., 229(8):2853–2865, 2010.

[15] A. Baraldi, M. S. Dodd, and A. Ferrante. A mass-conserving volume-of-fluid method: Volume tracking and droplet surface-tension in incompressible isotropic turbulence. Comput. Fluids, 96:322–337, 2014.

[16] S. B. Pope. Turbulent Flows. Cambridge Univ. Press, 2000.

[17] U. Schumann. Realizability of Reynolds-stress turbulence models. Phys. Fluids, 20:721, 1977.

[18] A. B. Aithal, M. Tipirneni, and A. Ferrante. Temporal accuracy of FastRK3. J. Comput. Phys., Under Review, 2022.

[19] A. Freund and A. Ferrante. Wavelet-spectral analysis of droplet-laden isotropic turbulence. J. Fluid Mech., 875:914–928, 2019.

[20] A. Freund and A. Ferrante. Large-eddy simulation of droplet-laden decaying isotropic turbulence using artificial neural networks. Int. J. of Multiphase Flow, page 103704, 2021.

[21] J. Towns, T. Cockerill, M. Dahan, I. Foster, K. Gaither, A. Grimshaw, V. Hazlewood, S. Lathrop, D. Lifka, G. D. Peterson, R. Roskies, J. R. Scott, and N. Wilkins-Diehr. XSEDE: Accelerating Scientific Discovery. Computing in Science & Engineering, 16(5):62–74, 2014.